Journal of Energy Resources Technology, Part A: Sustainable and Renewable Energy
asmedigitalcollection.asme.org | Journal archive available at: https://asmedigitalcollection.asme.org/energyresources

Computational Fluid Dynamics Analysis of Solidification in Baffled Molten Salt-Air-Cooled Heat Exchangers

Arun K. Raj[1]
Department of Civil and Mechanical Engineering,
Technical University of Denmark,
Kongens Lyngby 2800, Denmark
e-mail: arkra@dtu.dk

Nishith B. Desai
Department of Civil and Mechanical Engineering,
Technical University of Denmark,
Kongens Lyngby 2800, Denmark
e-mail: nbdes@dtu.dk

Fredrik Haglind
Department of Civil and Mechanical Engineering,
Technical University of Denmark,
Kongens Lyngby 2800, Denmark
e-mail: fhag@dtu.dk

Due to their high freezing point, molten salt heat exchangers face the problem of salt freezing during cyclic operation. As a result, it is critical to detect the onset of salt solidification and anticipate the phase change behavior in high-temperature heat exchange processes, since these parameters influence heat exchanger design and operation. This study presents a three-dimensional transient computational fluid dynamics analysis of a pilot-scale exchanger with molten salt on the tube side and air on the shell side. The investigation focuses on the effects of the baffle arrangement and initial molten salt temperature on the air outlet temperature, pressure drop, and the onset of salt solidification. The pressure–velocity field coupling and turbulence parameters were solved by employing a segregated solver algorithm and a realizable $k-\varepsilon$ turbulence model. Verification of the numerical model involved prior findings from a shell-and-tube heat exchanger using pure water as the shell-side fluid. The novel contribution of this work is to predict the time required for the molten salt to begin solidification within the tube bundle when air is used as the working fluid on the shell side of a single-segmented baffled shell-and-tube heat exchanger. The study concludes that, in the absence of a flow diverter, different baffle arrangements have minimal effect on the air outlet temperature or the start of salt solidification. A flow diverter, on the other hand, successfully slows solidification by distributing the flow, even when recirculation zones cause one-third of the heat exchanger length to remain ineffective. These findings provide a standard for future dynamic operation heat transfer assessments of molten salt-air-cooled heat exchangers. [DOI: 10.1115/1.4067898]

Keywords: baffles, computational fluid dynamics, phase change, solar salt, solidification, heat transfer, thermal energy storage systems

1 Introduction

Oil and gas, automotive, metallurgical, biopharmaceutical, chemical, food and beverage, textile, paper and pulp, and energy generation are just some of the industrial sectors that rely substantially upon the shell-and-tube heat exchangers (STHXs). These exchangers are valued for their considerable surface area relative to their volume and weight, their ability to be built in a variety of sizes for particular uses, the simplicity of repairing parts when they fail, and the well-recognized design and construction standards [1]. Despite these benefits, continuous research and development efforts concentrate on improving STHXs' durability, dependability, process optimization, energy efficiency, and adaptation to new technologies. Today, noteworthy changes are taking place in these sectors for molten salt STHXs. One common use is molten salt in concentrated solar power (CSP) facilities, where it functions as a heat transport fluid and a heat storage medium. In order to realize the full potential of molten salt heat exchangers, continuous efforts are required to overcome obstacles such as high temperatures, material compatibility, complicated fluid dynamics, corrosion, fouling, safety, and cost considerations.

Molten salts like solar salt ($NaNO_3$-KNO_3), Hitec salt ($NaNO_3$-KNO_3-$NaNO_2$), and Hitec XL® salt ($Ca(NO_3)_2$-KNO_3-$NaNO_3$) are preferred choices in CSP plants, nuclear power plants, and metallurgical industries. In CSP plants, molten salts are used both as a heat transport fluid and a heat storage medium, while in process heating and industrial applications, like steel heat treatment and annealing, molten salt STHX provides precise temperature control and uniform heat distribution, which are critical features for achieving the desired material properties. Furthermore, salts of carbonate, fluoride, and chloride are employed selectively according to the particular needs of industrial processes or applications. Prior research on the STHXs in molten salt may be roughly classified into shell-side and tube-side analyses, respectively. Research in these areas is still concentrated on fluid selection, operating conditions, and flow types (whether laminar or turbulent), as well as improvements in heat transfer through geometrical modifications like fins, ribbed tubes, turbulators, baffles, and coatings. Extensive research has been conducted on forced convective heat transport of molten salts within the tube bundle [2,3] and on their external flow

[1]Corresponding author.

Manuscript received August 28, 2024; final manuscript received January 24, 2025; published online February 28, 2025. Assoc. Editor: Tatiana Morozyuk.

around tube bundles [4,5] in STHXs. These studies have looked at how molten salts operate in both smooth and modified tube geometries at constant temperatures, constant heat fluxes, and a range of Reynolds numbers (whether in the laminar, transition, or turbulent regime). Nusselt number correlations for different operating situations have also been developed concurrently. As with previous investigations, the overall performance study of STHXs involving hot and cold fluids in counter, crossflow, and parallel configurations under different operating circumstances has also been reported [6–8]. A significant portion of these published studies concentrate on STHXs cooled by molten salt and liquids, with water and oil serving as the primary heat transport fluids [9].

In contrast, heat exchangers that transfer heat from molten salt to gases such as nitrogen, argon, helium, or air are generally more suitable for high-temperature applications like CSP, thermal energy storage systems, and waste heat recovery, compared to those that transfer heat from molten salt to oil. This is because gases can withstand higher temperatures than oils and are more affordable, ecologically friendly, and inert [10,11]. However, because molten salts have a very high melting temperature (~495 K for solar salt), their natural tendency to freeze is a major problem during the operation of molten salt STHXs. Unexpected weather patterns, pump blockages, heat tracing failure, and flow maldistribution are some of the inevitable causes of freezing that can happen while a plant is in operation. Thus, freeze protection measures must be put in place, even if they may raise parasitic costs like maintenance and operation. Since these parameters affect the construction and functionality of the STHX and the freeze prevention system, it is important to determine the start of solidification and forecast the phase transition characteristics of molten salts in high-temperature processes.

Most of the research on heat exchangers cooled by gas and molten salt concentrate on latent heat storage within concentric tubes or STHXs, which are commonly employed as storage units with stationary molten salt in the annular region. During their experimental studies, Han et al. [12] used a phase change material (PCM) contained within the annular gap of a double-pipe heat exchanger with air flowing through the inner pipe. Their results reported a greater influence on the phase change behavior during melting coming from the mass flowrate of air compared to the inlet temperature of air. Furthermore, as heat conduction alone dominates this phase transition, the effect of the mass flowrate decreases during solidification. Raj and Velraj [13] conducted a numerical analysis on a modular STHX unit, where air moved through tubes and PCM was allocated on the shell. PCM's solidification behavior, temperature distribution, and pressure drop were all evaluated in detail using both steady-state and transient-state analyses. Especially at lower air speeds, the air gap between STHX's two succeeding modules extends the air retention time, resulting in improved heat transfer. A similar analysis on the PCM is reported in Refs. [14,15].

Going beyond the storage standpoint, experiments on molten salt-gas-cooled heat exchangers have been conducted to evaluate and elucidate different heat transfer augmentation approaches. A eutectic mixture combination was used as the fluid inside the tubes in experimental studies on a gas-cooled STHX conducted by Qian et al. [10]. The energy exchange between the molten salt and shell fluids such as air (1 atm) and helium (5 atm) was examined independently. The findings indicated that while helium and air exhibited comparable thermal behavior, helium's superior thermophysical properties enabled it to perform more effectively as a coolant on the shell side. Qian et al. [11] examined the thermal characteristics in an STHX with finned tubes for molten salt to air, and in another STHX with segmented baffles for molten salt to salt. In both setups, the tube side contained hot molten salt, while the shell side had cold air or cooled molten salt. The study assessed both STHXs' performance at different intake fluid temperatures and mass flowrates. According to the findings, molten salt on the baffled shell-side transferred heat more effectively than other shell-side fluids like oil and air.

Over the past few decades, researchers have examined the problem of molten salt freezing in high-temperature reactors in addition to the numerous uses of STHXs in process industries. Chen et al. [16] investigated the temperature and velocity distributions on salt-to-air heat exchangers using both experimental and computational methods. In a fluoride-salt test loop, the salt passed through a network of serpentine tubes while air flowed from the bottom to the top. Experimental data were used to model and verify a time-dependent computational fluid dynamics (CFD) solution. Under varied load circumstances, the results showed a low probability of salt solidification. Additionally, the findings suggested that the potential risks of overcooling and solidification may be effectively minimized by regulating the air flowrate. Le Brun et al. [17] and Tiberga et al. [18] investigated coolant solidification and freeze-valve problems in high-temperature molten salt fast reactors. Identifying salt solidification, the design and implementation of freeze protection strategies, and the estimation of operation and maintenance (O&M) costs are of significant research interest. Kearney et al. [19] examined a parabolic trough solar field employing molten salt as the heat transfer fluid. The study focused on examining known critical issues such as salt solidification, proposing solutions, and estimating the overall cost involved with O&M. Additionally, the authors discussed different preheating methods and specific materials for pipes and fittings to avoid salt solidification. Similarly, González-Gómez et al. [20] pointed out that salt freezing could happen within the steam generators during CSP plant operations, when molten salt is used as the heat transfer fluid. Prieto et al. [21] evaluated the efficacy of heat tracing and impedance melting freeze protection strategies for a parabolic trough collector plant using molten salt as the heat transfer fluid. The findings suggested that impedance melting is ideal and emphasized the importance of employing freeze protection strategies to reduce the chances of salt freezing during plant operations.

Ozden and Tari [22] studied the effects of segmented baffles in a simplified STHX model, focusing on forced convection investigations using water as the shell-side medium. Representing the tubes as solid bodies, they utilized ANSYS FLUENT® to investigate the effects of baffles (i.e., varying cut and spacing) on pressure drop and heat transfer and also performed the sensitivity analysis of popular turbulence models, including the $k-\varepsilon$ model and the Spalart–Allmaras model, on the temperature and pressure drop at the shell outlet. The observations indicated that baffle cut had a major impact on the results. ANSYS FLUENT® was employed by Yang and Liu [23] in related numerical work to examine the heat transfer characteristics of water (shell-side) in a plate-baffled STHX. They found that while plate baffles increased pressure drop, they also enhanced heat transfer rates as compared to rod baffles. Pal et al. [24] used OPENFOAM 2.2.0 to investigate numerically the thermal performance of STHXs with and without baffles. Their comprehensive sensitivity study on turbulence models supported the findings of Ozden and Tari [22], and they recommended that for accurate heat exchanger solutions, to use the $k-\varepsilon$ turbulence model with y^+ larger than 15. Additionally, they pointed out how essential it is to consider the ratio of outlet length to velocity for efficient numerical stability, suggesting a ratio of at least 2.5. In a serpentine crossflow heat exchanger, Chen et al. [25] used heat transfer salt (KNO_3-$NaNO_2$-$NaNO_3$) distributed throughout a number of tubes to conduct comprehensive research integrating experimental and computational methods. Their tests, which were carried out at temperatures higher than 523 K to prevent salt solidification inside the tubes, demonstrated that variations in the air and molten salt mass flowrates significantly influenced the thermal characteristics.

The literature review reveals complications with the design and modeling of molten salt-gas-cooled heat exchangers and furthermore underscores that very few studies focus on identifying the molten salt solidification [19,20]. Prior research on shell-and-tube heat exchangers has mostly concentrated on elements like geometry modifications [11,16], working fluid selection [9,11,25], and flow configurations [6,8,16] in order to investigate their influence on

thermal performance; however, the phenomenon of molten salt solidification has not been thoroughly investigated. References [12,13] addressed the effects of solidification, specifically the overall time of solidification and/or melting, in which the working fluid (air) was positioned within the tubes as opposed to on the shell side. In industrial settings, such as process industries or CSP plants, it is essential to identify and forecast the early phases of solidification in the STHX. Early identification has a direct impact on the plant's smooth operation, financial consequences, and compliance with safety and economic standards.

This study examines a pilot-scale heat exchanger, where air cools the shell side and molten salt flows through the tube side, using a three-dimensional, transient CFD solver. The goal is to mimic the operating conditions of molten salt in pumped thermal energy systems or CSP facilities. The salt combination consists of 40% KNO_3 and 60% $NaNO_3$. The Boussinesq approximation was used to account for buoyancy effects caused by variation in temperature in the molten salt [26]. The relationship between pressure and velocity fields was repeatedly solved using a segregated solver technique, and turbulent viscosity and dissipation rates were captured using a realizable $k-\varepsilon$ turbulence model. Analysis was conducted under atmospheric pressure conditions. Prior findings from an STHX using water as the shell-side fluid were compared to the numerical model. We studied the impact of baffle arrangement and initial molten salt temperature on the outlet temperature, salt solidification, and pressure drop using a well-established standard CFD model with user-defined piece-wise linear functions for molten salt and air properties. Our research also seeks to determine how adding a flow diverter affects salt solidification within the STHX. The conclusions derived from this study provide actionable insights for practical heat exchanger design, such as selecting optimal baffle configurations and incorporating flow diverters to delay salt solidification.

Our work contributes to the following advancements:

(a) A study that determines when molten salt solidification starts inside the tube bundle by examining how air, acting as a working fluid, affects the shell side of the STHX. The localized areas of tube bundles that are most likely to result in salt solidification are specifically located. Prior research on molten salt-gas-cooled heat exchangers did not take salt solidification into account; instead, it concentrated on improving heat transmission [11,16,25]. Other research examined the use of air or different working fluids inside the tubes, together with molten salt as a static PCM on the shell side [12,13]. These studies estimated the total amount of time needed for melting and/or solidification inside the containment, but they did not identify particular regions inside the STHX that likely result in solidification.

(b) Evaluation of the impact of baffle arrangements (i.e., cut and number) on the initiation of solidification. Earlier research on STHX designs, either identical or different, focused on determining how baffle arrangements affected the outlet temperature employing various heat transfer fluids, including water or oil [9], while considering the tubes as solids [22,24].

(c) Evaluation of the presence of a flow diverter near the nozzle inlet to determine how it affects the initiation of solidification inside the tubes.

These findings serve as a foundation for future research on molten salt solidification during dynamic STHX operation and the development of practical freezing prevention techniques for these heat exchangers.

2 Methods

2.1 Computational Domain and Mesh. ANSYS DESIGN MODELER® (version 2023 R2), a commercial software program, was used to create the computational domain for this investigation. ANSYS MESHER® was used to generate the mesh. The mesh and geometry utilized in this investigation are shown in Fig. 1. According to the Tubular Exchanger Manufacturers Association (TEMA) guidelines, this simplified STHX geometry was created and verified by Ozden and Tari [22]. As shown in Fig. 1, we took into consideration that the tubes are packed with solar salt, whereas Ref. [22] depicted the tubes as solid bodies. Furthermore, Fig. 2 illustrates the STHX domain, including a flow diverter and its corresponding mesh. The flow diverter with 20 mm in width and 0.5 mm in thickness, is positioned 41 mm away from the centerline. Table 1 summarizes the geometric parameters of the STHX and the properties of the molten salt. References [12] and [27] provided the molten salt properties, whereas Span et al. [28] provided the air properties. A piece-wise linear function of temperature was used to incorporate both sets of properties. In Table 1, the property values within the specified range represent the lower and upper bounds of the linear interpolation used to calculate the properties at different temperatures. Carbon steel was used to make the tubes and shell.

Hexahedral and tetrahedral cells make up the majority of the computational mesh, whereas the tubes and main shell volume are composed of structured mesh elements. As shown in Fig. 1, inflation layers having y^+ value of approximately 20 were set close to the tube walls. This y^+ value was selected as the analysis does not involve flows with strong adverse pressure gradients or separation near the wall. Additionally, in order to limit the

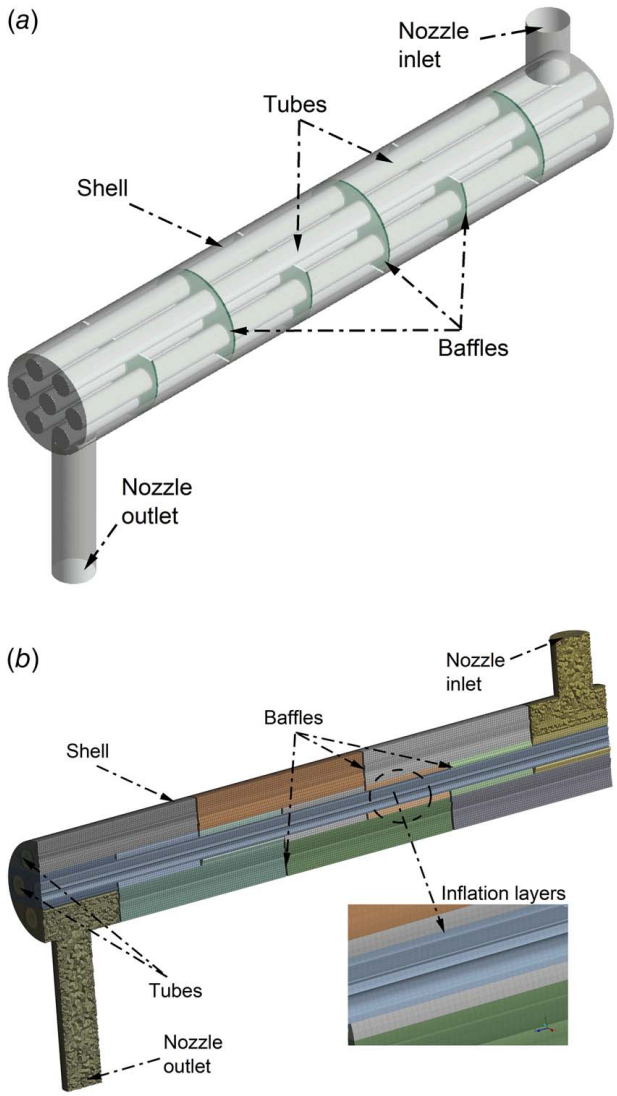

Fig. 1 (*a*) The STHX geometry and (*b*) the mesh structure employed for the current investigation

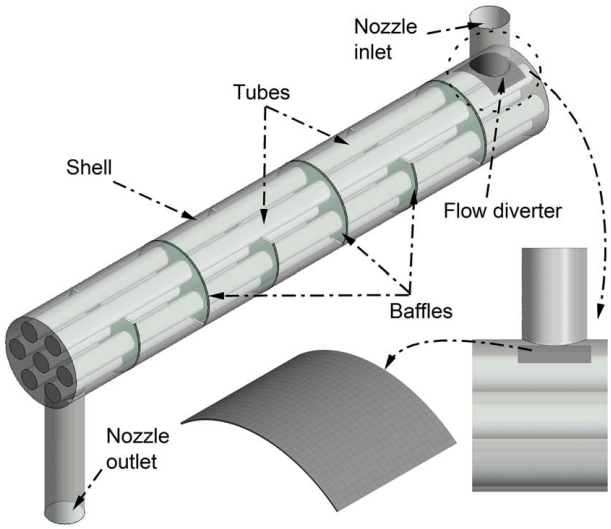

Fig. 2 Computational domain of the STHX with flow diverter

Table 1 The STHX dimensions and molten salt property

Parameter	Dimension		Property/Value
Shell outer diameter	90 mm		ρ (kg/m^3)
Shell length	600 mm		1931.10
Tube outer diameter	20 mm		C_p (J/kgK)
No. of tubes	7		1473.9–1525.5
Tube bundle geometry	Triangular		k (W/mK)
Tube pitch	30 mm	Molten salt	0.477–0.534
No. of baffles	6, 8, 10		μ (kg/m · s)
Central baffle spacing	86 mm		0.0076–0.00137
Baffle cut(s)	25%, 36%		T_s (K) and T_l (K)
Inclination angle	0 deg		494.83 and 508
Nozzle diameter	36 mm		L (kJ/kg)
Nozzle exit length	180 mm		100.9

computational time, a $y^+ \sim 20$ is a suitable value when used with the $k-\varepsilon$ turbulence model. This approach is supported by prior studies. For example, Pal et al. [24] performed CFD simulations of an STHX using OPENFOAM and recommended maintaining a minimum $y^+ \sim 15$ when employing $k-\varepsilon$ or SST $k-\omega$ turbulence approaches. A mesh convergence study was conducted to identify the appropriate mesh size. Following the recommendations in Refs. [22] and [24], the mesh size varies from 1.1 million to 1.6 million elements. The outlet temperature from the shell side was chosen as the parameter for evaluation. Three different mesh configurations were tested: 1,112,641 elements, 1,342,523 elements, and 1,557,986 elements; the results are illustrated in Fig. 3(*a*). The findings suggest a decrease in temperature at the outlet as time progresses across all scenarios. The values of air outlet temperature obtained using 1,342,523 and 1,557,986 elements have less than 0.05% deviation, indicating that further refinement has a negligible impact on the accuracy. Consequently, the mesh size of 1,342,523 elements was selected for all simulations ensuring satisfactory orthogonal quality and skewness while balancing computational cost and accuracy. To determine the optimal time-step for the transient simulations, a time independence study was conducted using step sizes of 0.25, 0.5, and 1.0 s. With an initial salt temperature of 573 K, the air outlet temperature was used as the comparison parameter, focusing on the six-baffle configuration. The findings are presented in Fig. 3(*b*). The results suggest that simulations with time-steps of 0.25, 0.5, and 1.0 s produce nearly identical results, i.e., deviation in air outlet temperature between the time-step size of 0.5 and 1.0 s at 300 s is 0.015%, confirming that the selected numerical scheme is sufficiently accurate for the chosen discretization. Based on this analysis, the largest tested time-step, 1.0 s, was adopted to minimize computational cost while maintaining solution accuracy.

2.2 Solution Methods. A three-dimensional Newtonian solver based on the pressure is employed, which combines the realizable $k-\varepsilon$ turbulence model with the conservation equations of mass, momentum, and energy in an unsteady state. For CFD modeling in STHXs, the realizable $k-\varepsilon$ turbulence model is favored over the standard $k-\varepsilon$ model due to its ability to give accurate dissipation rate predictions and turbulent viscosity calculations [24]. Ozden and Tari [22] conducted a detailed sensitivity analysis of various turbulence models, such as the $k-\varepsilon$ standard, $k-\varepsilon$ standard second order, $k-\varepsilon$ realizable, Spalart–Allmaras, and Spalart–Allmaras second order, and suggested that the $k-\varepsilon$ realizable model was the best choice for the simulation approach. Their work aimed at determining the shell-side heat transfer using water as the heat transfer fluid with varying baffle number and baffle cut. Pal et al. [24] employed the same geometry as Ozden and Tari [22] and conducted a sensitivity analysis of $k-\varepsilon$ standard and SST $k-\omega$ models. The findings suggested that both the $k-\varepsilon$ standard and SST $k-\omega$ models provide accurate predictions for temperature within ± 4%, respectively. Based on these works, the $k-\varepsilon$ turbulence model was chosen for the current investigation.

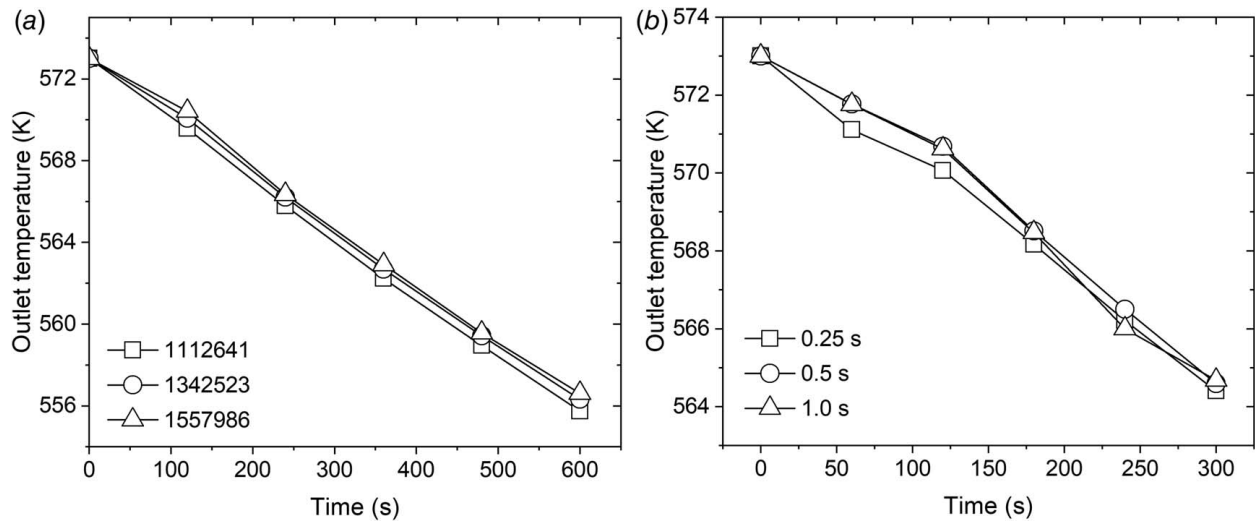

Fig. 3 (*a*) Mesh convergence study and (*b*) time convergence study

Because standard wall functions are less expensive to compute, they are chosen over enhanced wall treatment. The ANSYS Theory Guide [29] provides detailed explanations of turbulence models and transport equations.

In accordance with Ref. [22], to compute the relative shell-side pressure drop, an inlet mass flux condition is applied at the entrance to the nozzle, with a zero-gauge pressure outlet condition at the nozzle exit. In this work, the simulation begins with a steady-state analysis to establish approximate flow and temperature fields as an initial condition for the transient analysis. This step accelerates the duration needed for the system to transition to realistic transient conditions, ensuring computational efficiency and accuracy in capturing the transient thermal and flow behavior. In the steady-state analysis, the same geometry and inlet parameters (e.g., mass flowrate and initial temperature) as those used in the transient analysis are considered, and the resulting flow and temperature fields are then used to initialize the transient simulation. This approach prevents the system from starting from arbitrary initial conditions and allows the model to focus on capturing the transient onset of solidification and related phenomena from a physically consistent starting point. There is no heat flux, as it is assumed that the shell walls are totally insulated. For a comparison study, the starting temperatures in each of the seven tubes are between 543 K and 603 K, and each tube contains an equal volume of molten salt. In all test scenarios, at an inlet temperature and mass flowrate of 503 K and 0.00178 kg/s, respectively, air enters through the nozzle inlet. A no-slip boundary condition is implemented on all wall surfaces, and the tubes are modeled as smooth. Coupled walls are used to describe the interfaces between the tubes and the shell. The study excludes baffles, shell coverings, and flanges.

2.3 Numerical Schemes and Convergence. Pressure–velocity coupling is iteratively resolved by the numerical solver using a segregated solver technique, the semi-implicit method for pressure-linked equations [30]. The gradient discretization based on Green–Gauss node is more accurate than the cell-based approach [31]. First-order upwind discretization strategies are utilized to solve the momentum, energy, and turbulence parameters, while the pressure component is calculated using the pressure staggered option interpolation method. With the exception of energy, which is adjusted to 10^{-9} [29], all residuals are kept at their default control values, which are set to (10^{-6}). Based on the preliminary research using the model, a 1.0 s time-step is chosen to ensure computational stability and to track residuals. Tube volume is initialized with the correct molten salt temperature during solver initialization. Iteration convergences are checked continuously for temperature and solidification parameters using surface integrals and volume integrals monitor plots. Furthermore, flux and mass balances are routinely checked, and no imbalances have been found.

3 Results and Discussion

3.1 Solver Verification. The current CFD results were compared to results from an earlier validated CFD code for an STHX using pure water as the shell-side fluid in ANSYS FLUENT® (version 2023 R2) [22]. The findings presented in Ref. [22] were verified by comparison with theoretical works. Furthermore, the findings from Pal et al. [24] utilizing an identical STHX geometry as Ref. [22] used for verification. Based on our literature survey and the long-term objectives of our work, the STHX geometry proposed by Ozden and Tari [22] is a suitable choice for verification of our model. However, there are no earlier reported experimental works in the literature for such STHX configurations. In order to verify our code with another FLUENT-based code, our results were evaluated with those presented by Ozden and Tari [22]. Moreover, since inflation layers were not considered and the nozzle inlet and exit lengths were not specified in the work by Ozden and Tari [22], we also made a comparison with the results of an OPENFOAM-based code reported by Pal et al. [24] considering inflation layers.

Table 2 Comparison of current CFD results with reported works for an STHX with six baffles

$\dot{m}_w$ (kg/s)	CFD results		Ref. [24]	Ref. [22]	Relative percentage error (%)	
	$T_{w,o}$ (K)	Δp (Pa)	$T_{w,o}$ (K)	$T_{w,o}$ (K)	Ref. [24]	Ref. [22]
0.5	335.9	1367.7	336.8	340.4	0.27	1.32
1.0	332.6	5507.6	335.8	330.2	0.95	0.73
2.0	331.0	21,950.9	334.1	326.6	0.93	1.34

In our work, inflation layers were considered, and the nozzle inlet and exit lengths were decided upon based on the findings reported by Pal et al. [24]. Therefore, our work uses a different mesh resolution than that used by Ozden and Tari [22]. Deviations between our results and those obtained by Ozden and Tari [22] can thus be attributed to the use of different exit lengths and/or mesh. These reasons contributed to the observed minor deviations in results obtained from FLUENT [22] and OPENFOAM [24].

The findings from our CFD analysis are discussed in Table 2, which highlights the discrepancies between the obtained results and those of Pal et al. [24] and Ozden and Tari [22]. While Ref. [22] published findings for around 1.37 million cells, Ref. [24] compared the findings corresponding to 2.0 million cells for an identical STHX design and concluded that mesh convergence was obtained with about 1.2 million cells. Furthermore, Ref. [24] addressed issues not addressed in Ref. [22], such as inflation layers and maintaining a y^+> value larger than 15 for the analysis. Consequently, as Table 2 illustrates, at all water flowrates, a considerable variation in water temperature was seen between Ref. [22] and Ref. [24]. These factors contribute mainly to the observed differences between the FLUENT code and OPENFOAM code. However, the difference in the result between the codes is minimal. The unstructured mesh, which is made up of tetrahedral cells for verification, is shown in Fig. 4.

For the verification study, the exact same boundary conditions as those employed by Ref. [22] were used. The findings demonstrate that, for all mass flowrates, our CFD model, which has around 1.34 million cells, underestimates the shell outlet temperature (as shown in Table 2) in comparison to Ref. [22]. However, the study by Pal et al. [24] does not provide data corresponding to the shell-side pressure drop, and the measured deviation in outlet temperature is consistently below 1% for all flowrates. On the other hand, Ref. [22] overpredicts the outlet temperature for higher water flowrates, although the variation remains below

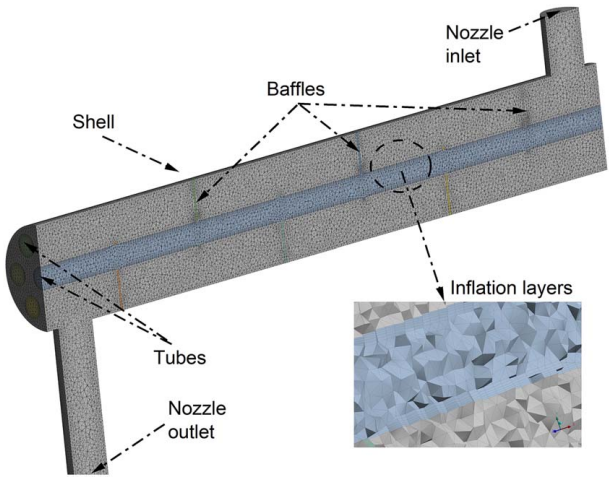

Fig. 4 Mesh used for the verification study

1.34%. It is also important to note that, at 2.0 kg/s flowrate, Ref. [22] indicates a pressure differential of around 25% with respect to the analytical data corresponding to Kern's technique and Bell Delaware methods. As explained in Ref. [24], the mesh improvement in our work reduces this pressure drop deviance to less than 16%. Since the entrance and/or exit length and nozzle inlet and/or outlet diameter were not specified by Ozden and Tari [22], the deviation in pressure drop can be attributed to the use of different geometric features of the STHX. Additionally, the pressure drop is highly dependent on the localized flow resistance (recirculation zones) and disturbances caused by geometry, especially for the STHX geometry with baffles. In contrast, the outlet temperature is a bulk phenomenon that is less affected by localized conditions. The aforementioned circumstances explain why the deviation in pressure drop (16%) is larger than that in outlet temperature (1.5%). According to our findings, the pressure drop deviation trend is comparable to that seen in Ref. [22]. Overall, the verification findings indicate that the outputs from our CFD model are rational and accurate.

3.2 Molten Salt Temperature. The study examines solar salt at three distinct starting temperatures: 543, 573, and 603 K. In the discharging cycles of pumped thermal energy storage systems and CSP plants, these are the typical operating temperature conditions [32,33]. Air flows into the nozzle inlet with a flowrate and temperature of 1.78×10^{-3} kg/s and 503 K, respectively. This flowrate complies with the TEMA-based general heat exchanger design guidelines [34]. The operating range, permitted pressure drop and velocity, and economic considerations relevant to STHXs are all covered by these guidelines [35]. Our research aims to ascertain how long it takes for solidification to start under such conditions. This is particularly important because, although the molten salt starts in a completely liquid state (with a liquid fraction of 1), the air temperature entering the nozzle is set just below the liquidus temperature (503 K compared to the liquidus temperature of 508 K for solar salt). By ensuring that solidification takes place gradually, this configuration enables us to track the temperature and liquid fraction profiles and pinpoint the exact instant at which the liquid transitions to a solid. The term "onset of solidification" describes the point where the molten salt temperature hits its freezing point, signifying the change from the liquid to the solid phase, rather than just the time required to attain a steady-state. By tracking both liquid fraction and temperature profiles, we can pinpoint the precise onset of solidification. For the sake of simplicity, all comparisons are done using the six-baffle arrangement with a 36% baffle cut and the solar salt's initial temperature is fixed at 573 K.

Figure 5 shows the changes in outlet temperature of air under different molten salt temperatures. The air temperature progressively drops from start (i.e., $t = 0$ s) to end (i.e., $t = 4800$ s) in each of the three studied scenarios. At regular intervals, the salt solidification—i.e., the point at which the volume-averaged value of liquid fraction (α) shifts from 1.0 (signaling the liquid phase) to 0.99 (signaling the solidification onset) inside the seven tubes—is tracked. The findings show that in all three cases, solidification starts when the salt temperature reaches 508 K, and the air outlet temperature reaches 512 K. The volume-averaged value of liquid fraction also drops from 1.0 to 0.99, as shown in Fig. 5. The time needed to trigger solidification, however, varies; Fig. 5 shows that for an initial salt temperature of 543 K, the required time is 3078 s (0.86 h); for an initial salt temperature of 573 K, it is 4196 s (1.16 h), and for 603 K, it is 4878 s (1.36 h). As anticipated, the duration before salt begins to solidify extends with higher initial temperatures of the molten salt.

Figure 6 shows the tube wall temperature contours at three distinct points in time. The initial salt temperature is 573 K in all scenarios. For consistency and ease of comparison, the temperature contour panel is fixed between 503 K and 534.8 K, respectively, for all three different times. Rather than focusing on a single tube,

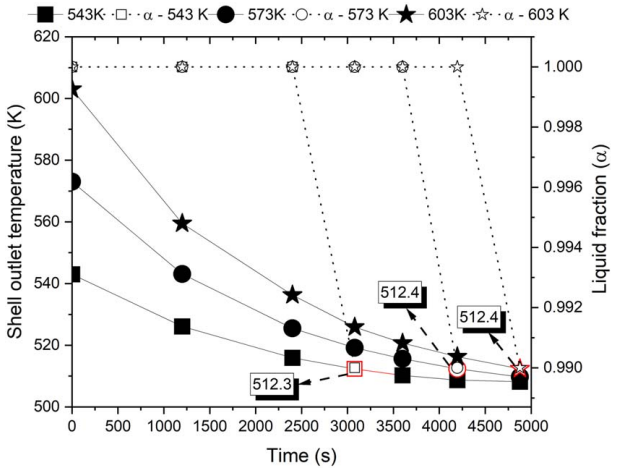

Fig. 5 Air outlet temperature and liquid fraction for an STHX with six baffles as a function of time

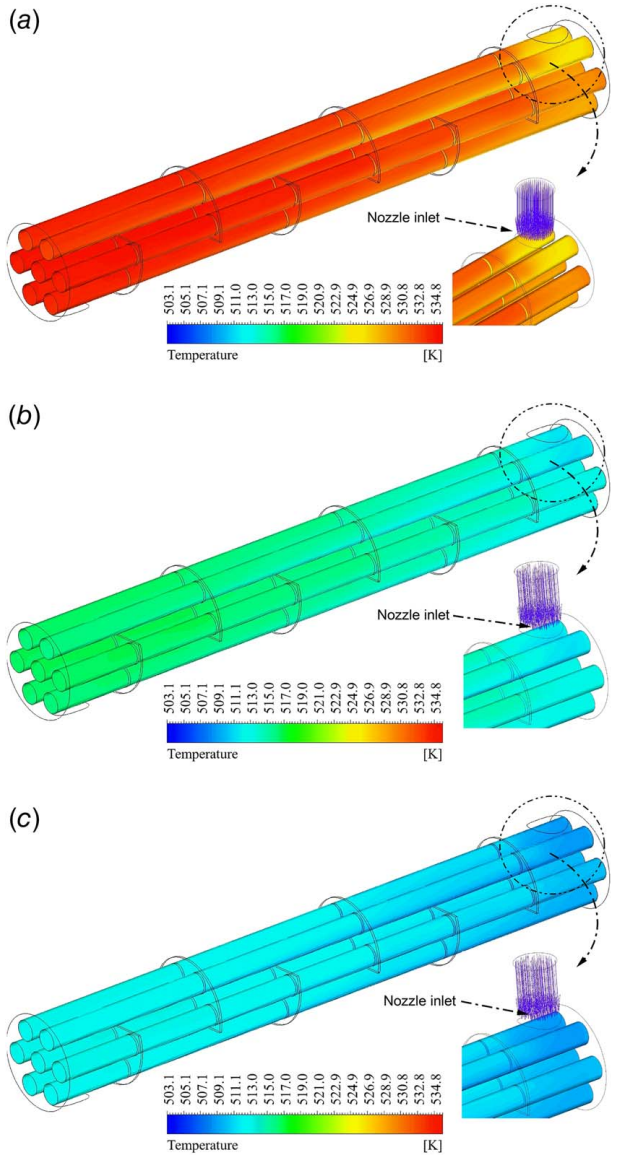

Fig. 6 Temperature contours for molten salt at 573 K and six baffles at various times: (*a*) 1800 s, (*b*) 3600 s, and (c) 4200 s

this analysis investigates the region near the nozzle inlet within the STHX that is more prone to salt solidification. This approach helps in optimizing operational parameters, such as the shell-side air velocity and molten salt inlet temperature, while avoiding the complexity of monitoring individual tubes. Initially, at 1800 s, the tube walls are at a higher temperature, ranging from 525 K to 534.8 K, as denoted by the reddish and slightly yellowish colors in Fig. 6(*a*). However, as time progresses, the tube wall temperature drops, falling below 512 K at 4200 s, as indicated by the bluish and light greenish colors in Fig. 6(*c*). Notably at 4200 s, the tube walls in the region close to the nozzle inlet (marked by the dotted lines) are already cooled below 508 K. This indicates the onset of salt solidification in this region, as confirmed by the volume-averaged liquid fraction values presented in Fig. 5. The contours in Fig. 6 align with the reported values shown in Fig. 5, indicating the temperature range between 508 K and 512 K at the tube exit corresponds to the initiation of salt solidification, confirming this process within the tubes in those areas. Due to the large temperature differential with respect to salt and air, the region near the nozzle inlet experiences the most heat transfer, making its location crucial. Because this phenomenon only happens in this specific area, it differs from the other regions of the tubes. The temperature contours on the *YZ* plane at three distinct periods are shown in Fig. 7. The results show that, in comparison to other tube parts, the cooling of salt occurs substantially quicker in the regions near the nozzle inlet, as shown in Fig. 6.

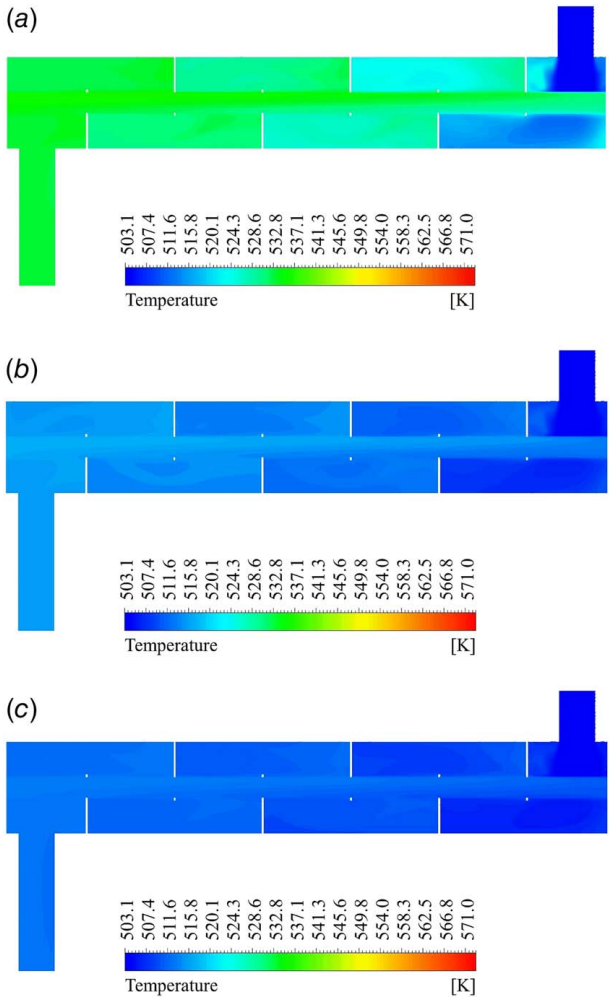

Fig. 7 Temperature contour profile for salt at 573 K with six baffles on the *YZ* plane at various time instances: (*a*) 1800 s, (*b*) 3600 s, and (*c*) 4200 s

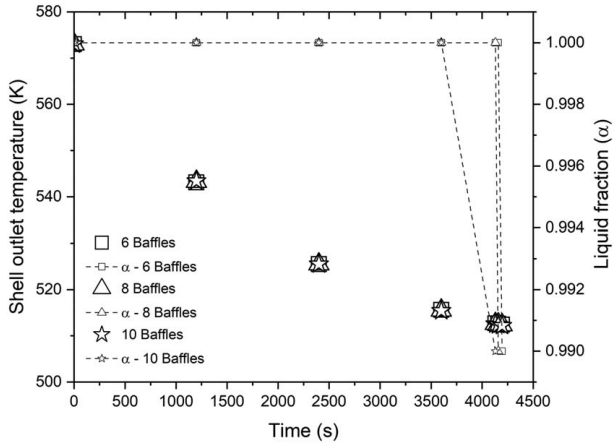

Fig. 8 Outlet temperature and liquid fraction for different baffle numbers

3.3 Baffle Number. Baffles are structural components that are commonly employed to enhance the effectiveness of the STHX. Additionally, they are employed to regulate the dynamics of the flow, which often results in the formation of recirculation zones where the fluid rotates and/or swirls. The fluid's direction and velocity alter as it gets closer to the baffles, creating recirculation zones. Recirculation eddies or vortices develop inside these zones, boosting fluid mixing and, in turn, heat transmission [36].

Prior research employing the same or comparable STHX geometries has mostly concentrated on water and oil as the working fluids for the shell side [7,22,24]. The present work aims to (a) compute how changing the number of single-segmented baffles affects the salt solidification, and (b) calculate the pressure differential in the STHX employing molten salt and air. Understanding the pressure differential for a varying number of baffles is essential for developing practical methods to stop salt solidification, as pressure drop is dependent on fluid density and other variables.

Figure 8 shows the outlet temperature for various baffle arrangements with a fixed baffle cut of 36%. The findings convey that varying baffle numbers, in contrast to the initial salt temperature (see Fig. 5), have very small impact on the solidification onset. In particular, for the STHX designs with six, eight, and ten baffles, solidification starts around 4196 s (1.16 h), 4158 s (1.16 h), and 4130 s (1.15 h), respectively. When geometry, operating parameters, and boundary conditions are the same, the initiation of salt solidification is not significantly affected by the number of baffles. This negligible effect is due to the low density, as well as the low heat capacity and low thermal conductivity of air, highlighting the necessity of looking for alternative baffle shapes in order to improve the heat transfer. Although increasing the baffle count improves localized heat transfer, the overall heat transfer remains limited by the low thermal conductivity, specific heat, and density of air. Furthermore, the findings show that for all three arrangements, solidification starts when the air outlet temperature approaches 512 K, and the air temperature decreases for all tested configurations. Notably, the initiation of solidification happens slightly earlier for the ten-baffle configuration compared to the six-baffle configuration. However, the differences in solidification onset times are marginal. To understand this behavior better, it is necessary to investigate the flow physics associated with variations in baffle numbers. Additionally, the findings of previous works align with the observations made in the present work. For example, experimental studies were carried out by Habib et al. [37] to examine the turbulent flow properties of air passing through a duct with segmented baffles. The findings showed that the addition of the baffles resulted in a far greater increase in pressure drop than in the heat transfer coefficient. Additionally, the findings indicated that only a slight improvement in heat transfer might be anticipated for

fluids like gases that have low heat transfer coefficients. Wang et al. [38] conducted a comparative study on three configurations of STHXs: STHX with segmented baffles, STHX with continuous helical baffles, and STHX with staggered baffles. Using water as the shell-side fluid, their findings indicated that segmented baffles were not optimal for heat transfer enhancement and often resulted in higher pressure drops without significant heat transfer benefits. Figure 9 depicts the streamtubes for the various baffle types. As mentioned earlier, air changes direction and velocity as it strikes the baffles, which prevents the region behind the baffles from being used efficiently for crossflow. Recirculation zones are therefore visible in certain areas (shown by dark dotted circles). When there are six baffles, this behavior is more common. However, as shown in Fig. 9, the airflow seems to be fully developed as the baffle count rises to ten, and the crossflow zone extends up to the area between the sixth and seventh baffles. The findings show that the pressure drop for the STHX design with six, eight, and ten baffles is 1734.3, 1748.1, and 1764.1 Pa, respectively. This increased development of airflow and extended crossflow likely results in slightly earlier solidification.

As anticipated, as the baffle number increases, so does the pressure drop. This trend is in line with the results shown in Ref. [22], which showed that upon utilizing pure water, as the number of baffles increased, the pressure drop also increased significantly.

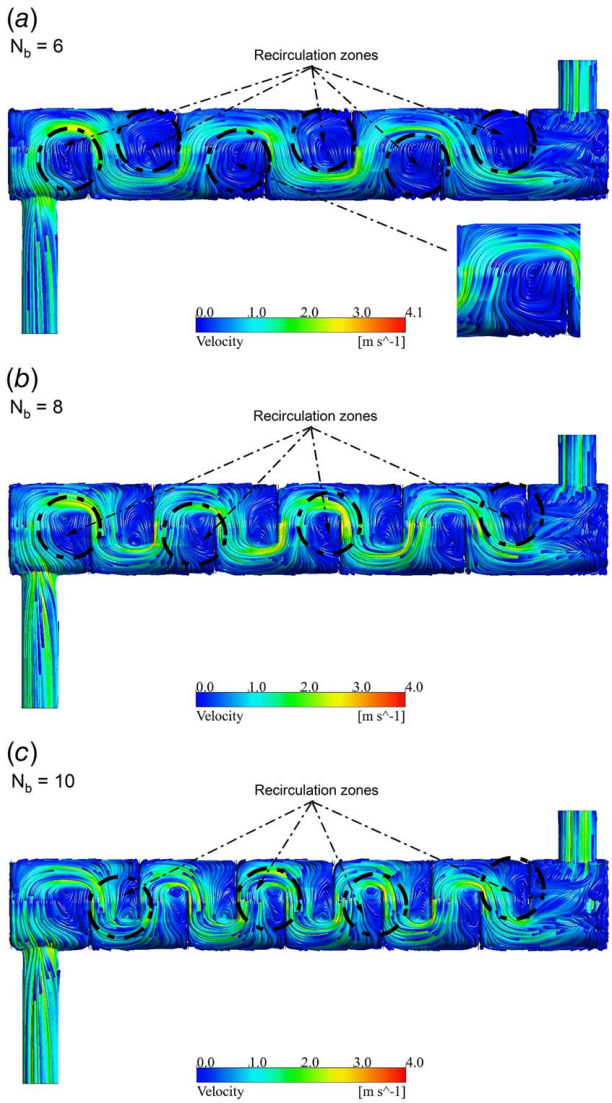

Fig. 9 Streamtubes for molten salt at 573 K with varying baffle numbers

From the standpoint of heat transfer, an STHX layout with ten baffles seems to be more advantageous than alternative configurations, especially when taking into account the well-developed airflow zone seen in Fig. 9 and a marginal rise in pressure drop. The existence of recirculation zones indicates that about one-third of the exchanger length, particularly near the shell nozzle exit, is inefficient in assisting with heat transfer for all baffle configurations. This analysis involves single-segmented baffles within the STHX configuration, which enables establishing a baseline understanding of the onset of solidification and flow physics in the presence of these standard baffle designs. However, to develop an effective STHX, further analyses exploring different baffle configurations, such as double-segmented, helical, rod-shaped, disk-and-doughnut, perforated, inclined or angled, chevron, and mesh baffles, are recommended.

3.4 Baffle Cut. The design and configuration of the baffles within the shell, as illustrated in Fig. 10(*a*), significantly affect the energy exchange between the fluids and the overall pressure loss within the STHX. This design also influences other parameters such as fluid velocity, mixing, and residence duration. The outlet temperature is shown for two distinct baffle cut arrangements (25% cut and 36% cut) in Fig. 10(*b*). The molten salt, in both situations, starts at a temperature of 573 K. According to the findings, both baffle cuts show a gradual drop in exit air temperature. Furthermore, for both baffle cuts, solidification always starts once the outlet temperature hits 512 K. The findings indicate that the 25% baffle cut had a slightly delayed start of solidification, beginning at 4236 s (1.18 h), as compared to 4196 s (1.16 h) for the 36% baffle cut. In essence, under the same geometry and operating conditions, changing the baffle cut shows little or negligible impact on the start of solidification. The streamtubes for various baffle cuts are shown in Fig. 11, which confirms the findings shown in Fig. 10(*b*). The circular regions in Fig. 11 clearly portray that the flow is not evenly distributed because of larger recirculation zones when the baffle cut is decreased to 25%. This might account for the relatively delayed start of solidification with the 25% baffle cut as the region downstream is not effectively utilized for crossflow. Conversely, a comparison with the findings from Ref. [22], which employed pure water, illustrates that a smaller baffle cut slightly improves the overall heat transfer. Additionally, at 2.0 kg/s flowrate, the results in Ref. [22] depict that reducing the baffle cut increased the heat transfer rate by no more than 8%. Furthermore, the restricted flow area for the decreased baffle cut causes the velocity to rise in the areas close to the baffle cut.

In accordance with the findings of the investigation carried out with water on the shell side in Ref. [22], the shell-side pressure drop for the 25% baffle cut (1789.6 Pa) is higher than that for the 36% baffle cut (1734.3 Pa). The recirculation zones that emerge in the molten salt-air STHX and the intrinsically poor thermophysical characteristics of the air may be the cause of the lack of improvement in heat transfer with the modifications to the baffle cut.

3.5 Flow Diverter. Prior research on phase change energy storage [12,39,40] sought to shorten the energy storage material's solidification and/or melting time. This approach is ideal for systems that prioritize quick energy cycling, where fast phase changes are crucial for efficient operation. However, molten salt-air STHXs have different operational requirements. These systems must operate continuously and reliably for extended periods with minimal maintenance. In such systems, delaying the onset of solidification is necessary to avoid issues such as blockages, scaling, or uneven heat transfer, which can arise if solidification occurs too early during operation. As was previously mentioned in Secs. 3.3 and 3.4, reducing the baffle number and/or baffle cut leads to increasing the time required for solidification onset within the STHX. This helps us choose the heat exchanger geometry with six baffles and a 25% cut, in line with our objective.

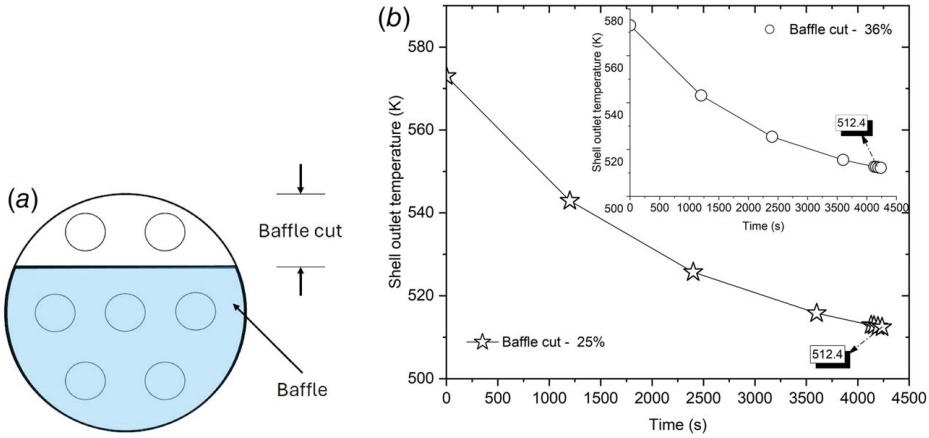

Fig. 10 (*a*) Baffle cut and (*b*) outlet temperature for two distinct baffle cuts

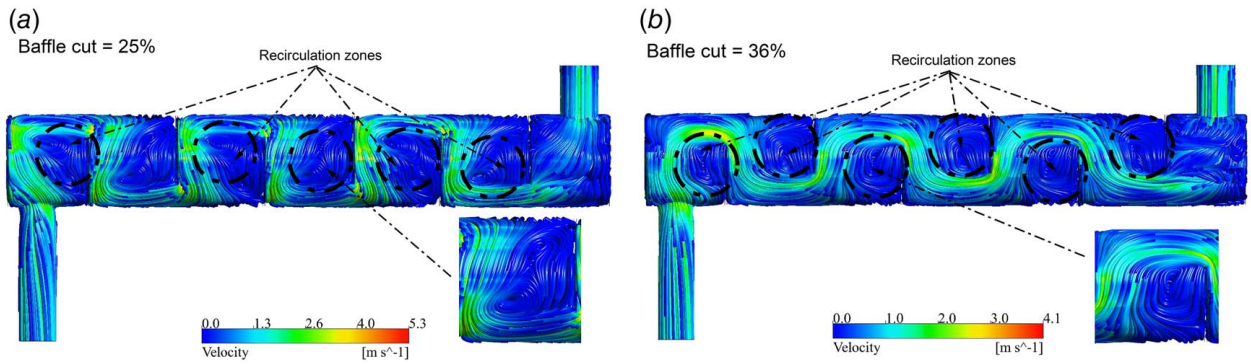

Fig. 11 Streamtubes for molten salt at 573 K corresponding to various baffle cuts

Furthermore, the tube areas near the nozzle inlet are more vulnerable to solidification, according to results derived from Figs. 6 and 7. Changes in baffle cut or number have no effect on this characteristic. Although there will likely be a cost in pressure drop, which is frequently proportionate to the intricacy of the baffle design, altering the baffle shape should improve heat transfer. This further restricts our focus to investigating novel baffle designs while keeping the single-segmented baffles for further evaluation. Given the need for distributing the flow while minimizing the thermal gradients caused by temperature differences in localized tube regions nearer the nozzle inlet, a flow diverter is added, as shown in Fig. 2. The flow diverter's function is to distribute the airflow around the tubes. It does not directly enhance or deteriorate heat transfer but serves to prevent direct impingement of air on the upper tube rows, which are more susceptible to salt solidification. All of these challenges motivate us to investigate further as follows:

(a) Does the onset of solidification get delayed if the baffle number is decreased?
(b) Is it possible for a flow diverter to reduce the susceptibility of the tube areas near the nozzle inlet to salt solidification?

Table 3 enables examination of the various arrangements of the central baffle spacing. Figure 12 shows the solidification time

Table 3 Baffle spacing across different studied configurations

Baffle number	Baffle spacing (cm)
2	198.67
4	118.4
6	86
10	47

with and without baffles for various baffle arrangements (i.e., $N_b = 2$, 4, 6, and 10). Remarkably, adding the flow diverter resulted in an increased duration for the phase change process across all baffle configurations compared to the STHX geometry without the diverter. The STHX with six baffles, 25% cut, and without a flow diverter started to solidify in 4236 s (1.18 h), while the duration increased to 4359 s (1.21 h) when a diverter was included. These observations support the idea that including a flow diverter postpones solidification by distributing the flow more effectively. It is particularly significant that this accomplishment is made possible by a small but straightforward change to the STHX. Figure 13 displays the vector plots for the tested heat exchanger configurations, both with and without a flow diverter. It is clear from the arrangement without a flow diverter that the upper tube rows are immediately impacted by the incoming air flow, which speeds up the energy transfer in these sections. In contrast, as shown in Fig. 13(*b*), the arrangement with a flow diverter ensures that the flow from the nozzle inlet does not immediately impinge on the upper row tubes by distributing the incoming air flow throughout the tube sections. This redistribution enhances mixing, thereby improving the local convective heat transfer. Improved mixing generally enhances heat transfer rates, because it prevents the formation of stagnant zones where heat is not efficiently transferred. However, higher heat transfer rates do not always result in a faster onset of solidification. The reason is that increased mixing distributes the heat more evenly across the tube surfaces, which reduces the temperature gradient near the tube walls. The gradual temperature drop delays the point at which the salt reaches its solidification temperature. In essence, increased heat transfer (due to better mixing) helps delay solidification, because it slows down the cooling rate in the region near the tube walls, where solidification is most likely to occur. As observed from Fig. 13(*b*), inclusion of a flow diverter causes an increase in

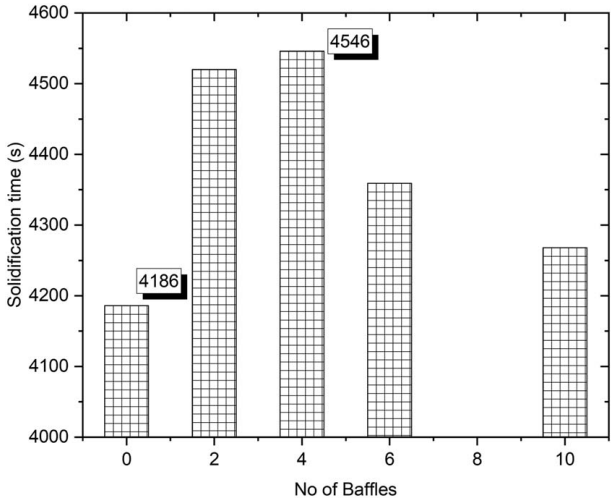

Fig. 12 Solidification time for the STHX with flow diverter for different baffle numbers

velocity close to the surrounding regions even if it lengthens the onset to solidification. In terms of pressure loss, earlier data without a flow diverter indicated 1789.6 Pa; however, incorporating a flow diverter results in a slightly higher pressure loss (1806.23 Pa), representing just a 1% increase, which is reasonable. Additionally, the previously reported findings show that adding a flow diverter close to the nozzle inlet has no effect on heat transfer.

Furthermore, the STHX geometry with four baffles, 25% cut, and with a flow diverter delays the initiation of solidification to 4546 s (1.26 h), according to the data illustrated in Fig. 12. On the other hand, the commencement of solidification occurs sooner in the STHX geometry without baffles (i.e., 4186 s), but the solidification time for the two-baffle configuration lies between the instances with and without baffles and with a four-baffle configuration. Remarkably, when compared to previously documented incidents without a flow diverter, the STHX geometry comprising a flow diverter without baffles exhibits a relatively faster solidification onset. This implies that air flowing through the shell side makes it easier to exchange energy with the tubes filled with molten salt when there are no baffles. Despite the fact that baffles are designed to enhance heat transfer by creating turbulence, here with the working fluid and operating parameters, the baffles might impede the fluid's flow path and create disruptions, which would prevent energy exchange. Furthermore, the effect of baffles on flow distribution is severely undermined by the weak thermophysical characteristics of air, primarily its low density. Because the solidification time is reduced in all other cases (e.g., 4268 s (1.19 h) for the ten-baffle arrangement with a flow diverter), these conclusions hold true for two- and four-baffle arrangements. This suggests that baffles are useful for creating turbulence and facilitating energy exchange. At the same time, because it delays the start of solidification, the STHX geometry consisting of four baffles along with 25% baffle cut is better amongst the evaluated arrangements for accomplishing our goal. In this configuration, the corresponding pressure drop is 1775.76 Pa.

The temperature contours of the tube walls containing molten salt (573 K) after 4200 s for various baffle arrangements and no baffles

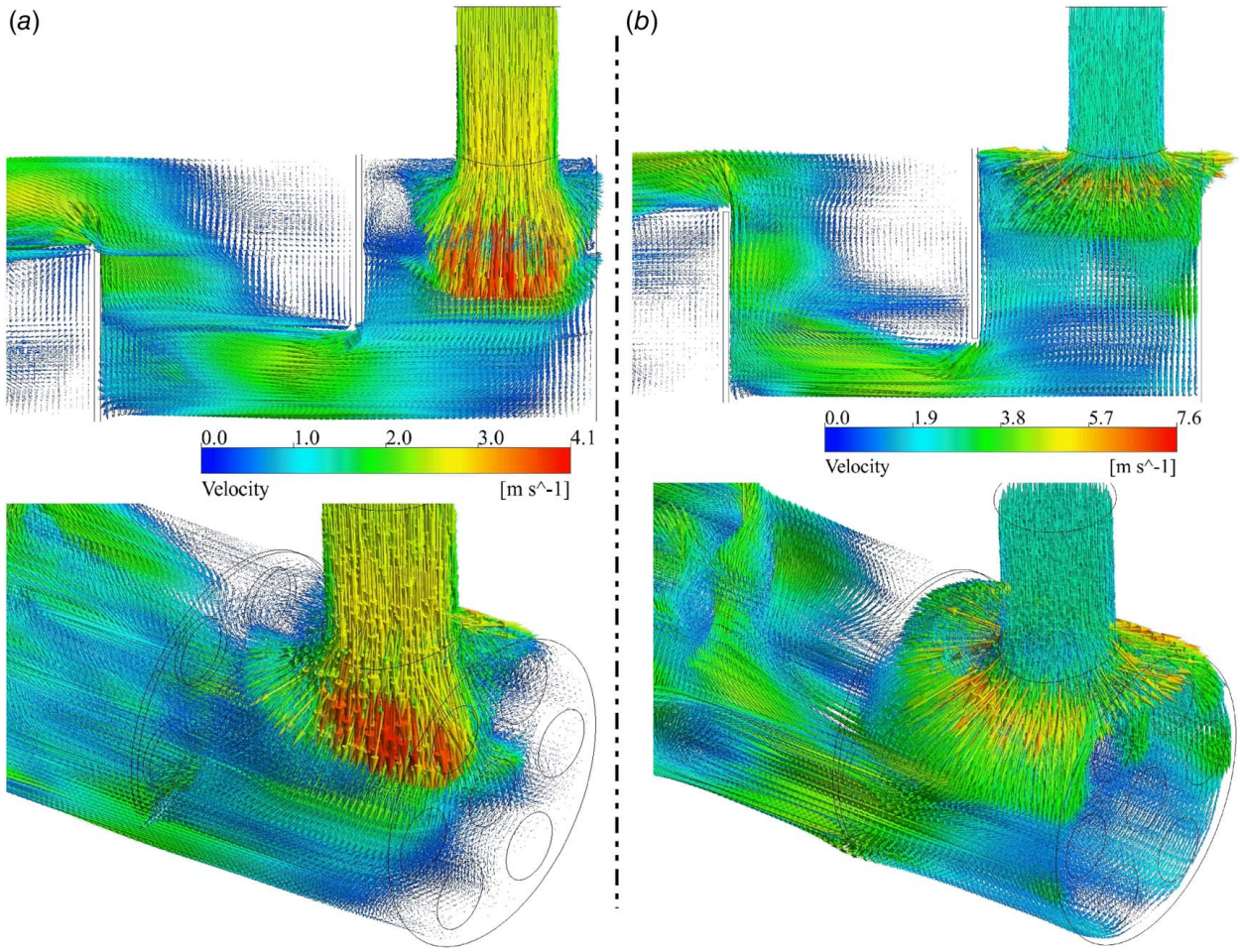

Fig. 13 Vector plots for 25% baffle cut with and without a flow diverter: (*a*) without flow diverter and (*b*) with flow diverter

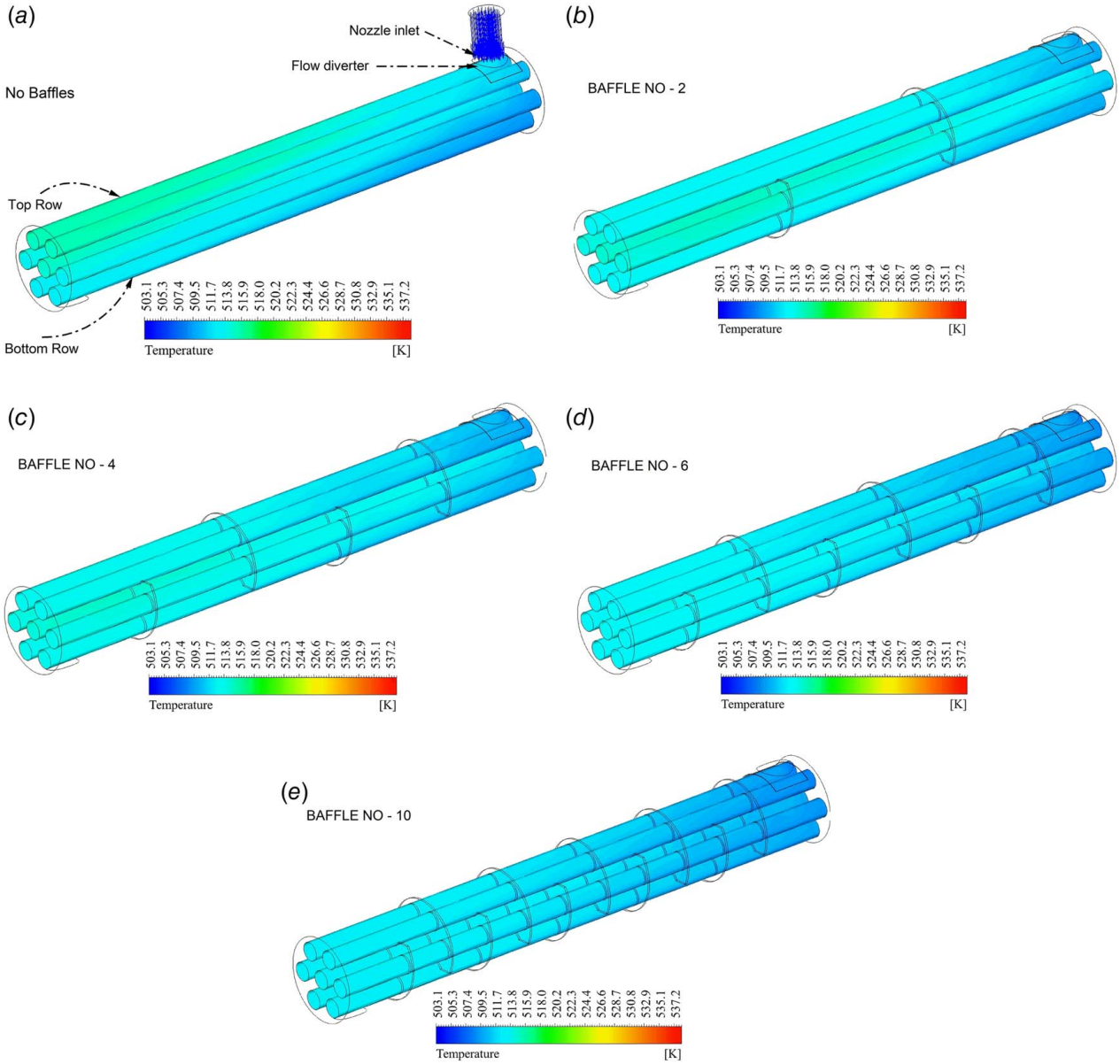

Fig. 14 Temperature contours for various baffle arrangements with a flow diverter

are shown in Fig. 14. For ease of comparison, all vector plots, contours, and streamtubes are scaled to the same size and variable range. The contour plots in Fig. 14 that have green (higher temperature regions) and blue (lower temperature regions) are the main subjects of this discussion. Here, 524.4–515.9 K is the high-temperature range, and 509.5–513.8 K is the low-temperature range. With the exception of the no-baffle configuration, where solidification starts early at 4186 s, the tubes in the bottom row of all examined baffle arrangements reach 512–513 K (blue shades) at 4200 s, suggesting that solidification starts earlier.

In contrast to the other examined designs, the contour plots for the six-baffle and ten-baffle configurations simultaneously reveal the least amount of green shades, suggesting that these baffle arrangements promote better energy exchange. The least blue colors, on the other hand, are seen in the two- and four-baffle designs, indicating that these baffle arrangements obstruct the flow in a way that prevents energy exchange. Furthermore, for both the two-baffle and four-baffle arrangements, the high-temperature areas are centered close to the center tube rows. The solidification time data shown in Fig. 12 support these results, demonstrating that a four-baffle arrangement takes the longest time (4546 s) whereas a ten-baffle arrangement takes the shortest time (4268 s). A mixture of green and blue hues, on the other hand, is seen in the baffle-free scenario, suggesting a progressively decreased energy transfer from the nozzle inlet to the exit as a result of uniform flow without baffles. STHXs typically exhibit this characteristic.

Tubes and streamtubes have temperature contours within the shell, and these are shown in Fig. 15, which compares STHX designs with and without a diverter, four baffles, and a 25% baffle cut. Salt solidification starts after 4546 s (1.26 h) for the instance with a flow diverter and 4269 s (1.19 h) for the instance without a flow diverter. Interestingly, the energy transfer between the air and salt is more noticeable in the tube regions near the main flow (shown by streamtubes in the magnified regions in Fig. 15) than in the regions adjacent to the recirculation zones. A shade of green at the inlet gives way to a red shade at the exit, indicating a reduction in energy transfer along the entire length of the heat exchanger in both cases. As mentioned earlier, a flow diverter helps to re-distribute the flow near the tubes closer to the nozzle inlet, slowing down the solidification process without affecting energy transfer. In the case of pressure drop, the finding shows

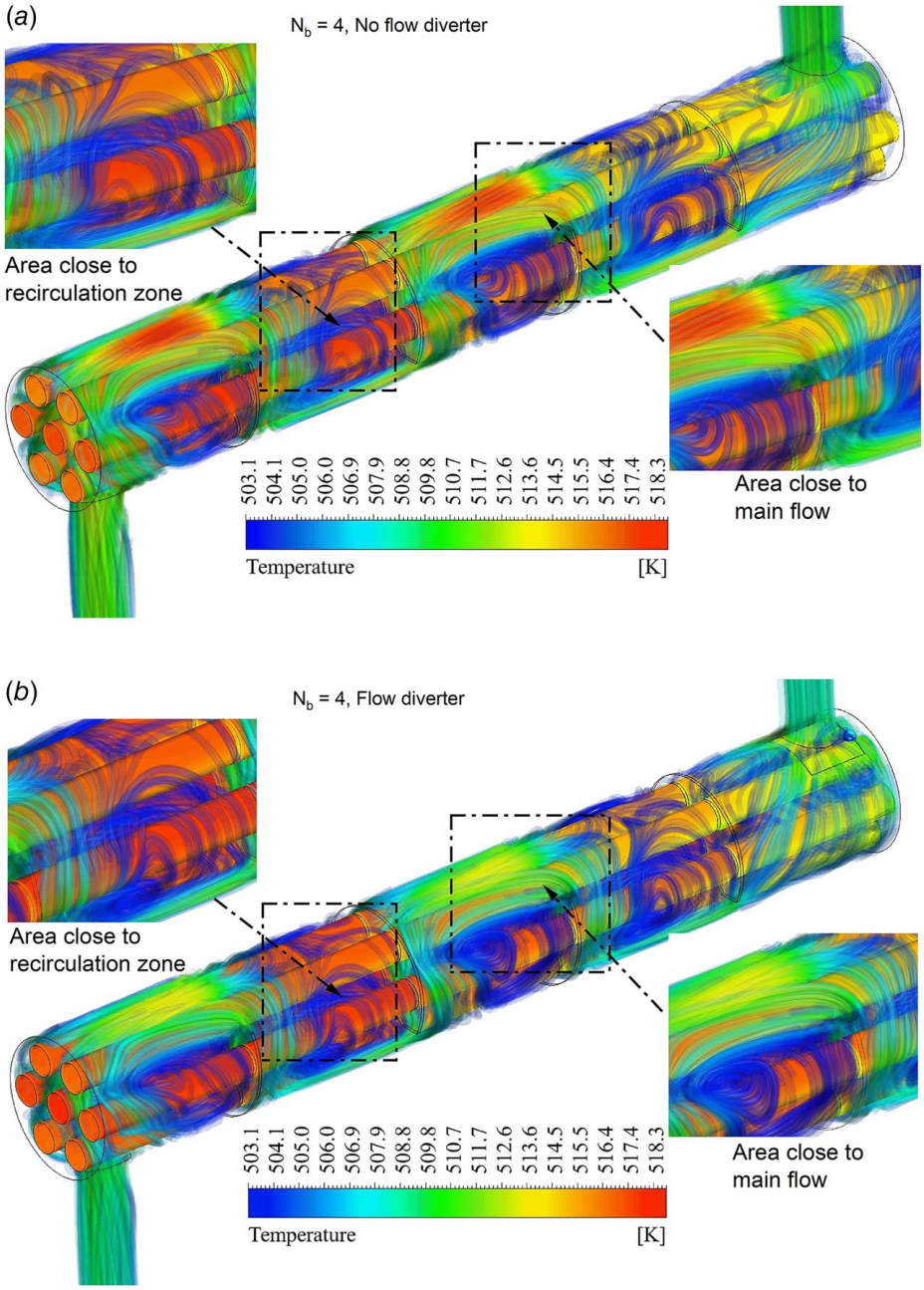

Fig. 15 Streamtubes and temperature contours for molten salt at 573 K with a 25% baffle cut

that adding a flow diverter only slightly increases it (about 1%) when compared to the STHX configuration without one. Thus, the four-baffle arrangement featuring a 25% baffle cut and a flow diverter efficiently delays the start of solidification with minimal impact on pressure drop and energy exchange.

4 Conclusions

This paper presents the effects of a molten salt-air heat exchanger, focusing on identifying salt solidification inside the tubes when air is used on the shell side. We also evaluated how different baffle arrangements affect the outlet temperature of the air and the pressure loss, and investigated how incorporating a flow diverter could delay the solidification of salt. According to the results, the higher the initial salt temperature, the longer it took for solidification to start. Without a flow diverter, the results indicated that both baffle number and baffle cut did not affect the solidification time for the studied baffle arrangements. Nevertheless, in comparison to other baffle arrangements without a flow diverter, the STHX geometry with a flow diverter helped postpone the onset of salt solidification. Out of the investigated configurations, the STHX geometry containing four baffles with 25% baffle cut served as the best option for achieving the study objectives. Furthermore, the formation of recirculation zones led to approximately one-third of the heat exchanger's overall length being underutilized in all examined configurations.

Acknowledgment

The research presented in this paper was funded by the European Union research and innovation program Horizon Europe under the Marie Skłodowska-Curie Actions Postdoctoral Fellowship (MSCA-PF) Grant agreement No. 101111194. The financial support is gratefully acknowledged and funded by the European

Union. Views and opinions expressed are those of the authors only and do not necessarily reflect those of the European Union. Neither the European Union nor the granting authority can be held responsible for them.

Conflict of Interest

There are no conflicts of interest.

Data Availability Statement

The datasets generated and supporting the findings of this article are obtainable from the corresponding author upon reasonable request.

Nomenclature

k = thermal conductivity (W/m/K)
L = latent heat (J/kg)
C_p = specific heat capacity (J/kg/K)
N_b = number of baffles
T_m = solidus temperature (K)

Greek Symbols

μ = dynamic viscosity (kg/m/s)
ρ = density (kg/m^3)

Abbreviations

CFD = computational fluid dynamics
CSP = concentrated solar power
PCM = phase change material
STHXs = shell-and-tube heat exchangers
TEMA = Tubular Exchanger Manufacturers Association

References

[1] Mahmoudinezhad, S., Sadi, M., Ghiasirad, H., and Arabkoohsar, A., 2023, "A Comprehensive Review on the Current Technologies and Recent Developments in High-Temperature Heat Exchangers," Renew. Sustain. Energy Rev., **183**, p. 113467.
[2] Bin, L., Yu-Ting, W., Chong-Fang, M., Meng, Y., and Hang, G., 2009, "Turbulent Convective Heat Transfer With Molten Salt in a Circular Pipe," Int. Commun. Heat Mass Transfer, **36**(9), pp. 912–916.
[3] Lu, J., Sheng, X., Ding, J., and Yang, J., 2013, "Transition and Turbulent Convective Heat Transfer of Molten Salt in Spirally Grooved Tube," Exp. Therm. Fluid. Sci., **47**, pp. 180–185.
[4] Yu-Ting, W., Bin, L., Chong-Fang, M., and Hang, G., 2009, "Convective Heat Transfer in the Laminar–Turbulent Transition Region With Molten Salt in a Circular Tube," Exp. Therm. Fluid. Sci., **33**(7), pp. 1128–1132.
[5] He, S., Lu, J., Ding, J., Yu, T., and Yuan, Y., 2014, "Convective Heat Transfer of Molten Salt Outside the Tube Bundle of Heat Exchanger," Exp. Therm. Fluid. Sci., **59**, pp. 9–14.
[6] Fetuga, I. A., Olakoyejo, O. T., Abolarin, S. M., Gbegudu, J. K., Onwuegbusi, A., and Adelaja, A. O., 2023, "Numerical Analysis of Thermal Performance of Waste Heat Recovery Shell and Tube Heat Exchangers on Counter-Flow With Different Tube Configurations," Alexandria Eng. J., **64**, pp. 859–875.
[7] Wang, S., Wen, J., and Li, Y., 2009, "An Experimental Investigation of Heat Transfer Enhancement for a Shell-and-Tube Heat Exchanger," Appl. Therm. Eng., **29**(11–12), pp. 2433–2438.
[8] Abd, A. A., Kareem, M. Q., and Naji, S. Z., 2018, "Performance Analysis of Shell and Tube Heat Exchanger: Parametric Study," Case Stud. Therm. Eng., **12**, pp. 563–568.
[9] Du, B. C., He, Y. L., Wang, K., and Zhu, H. H., 2017, "Convective Heat Transfer of Molten Salt in the Shell-and-Tube Heat Exchanger With Segmental Baffles," Int. J. Heat Mass Transfer, **113**, pp. 456–465.
[10] Qian, J., Kong, Q., Zhang, H., Huang, W., and Li, W., 2016, "Performance of a Gas Cooled Molten Salt Heat Exchanger," Appl. Therm. Eng., **108**, pp. 1429–1435.
[11] Qian, J., Kong, Q. L., Zhang, H. W., Zhu, Z. H., Huang, W. G., and Li, W. H., 2017, "Experimental Study for Shell-and-Tube Molten Salt Heat Exchangers," Appl. Therm. Eng., **124**, pp. 616–623.
[12] Han, Z., Wickramaratne, C., Goswami, D. Y., and Jotshi, C., 2022, "Experimental Study on Operating Characteristics of Nitrate Salt-Based Latent Heat Thermal Energy Storage Unit," Appl. Therm. Eng., **202**, p. 117846.
[13] Raj, V. A. A., and Velraj, R., 2011, "Heat Transfer and Pressure Drop Studies on a PCM-Heat Exchanger Module for Free Cooling Applications," Int. J. Therm. Sci., **50**(8), pp. 1573–1582.
[14] Ramos Archibold, A., Bhardwaj, A., Rahman, M. M., Yogi Goswami, D., and Stefanakos, E. L., 2016, "Comparison of Numerical and Experimental Assessment of a Latent Heat Energy Storage Module for a High-Temperature Phase-Change Material," ASME J. Energy Resour. Technol., **138**(5), p. 052007.
[15] Ismail, K. A., Leitão, A. B., Lino, F. A., and Henriquez, J. R., 2021, "Parametric Study of the Solidification Process Between Vertical Parallel Plates of a Storage System," ASME J. Energy Resour. Technol., **143**(7), p. 070903.
[16] Chen, Y.-S., Tian, J., Zhu, H.-H., Fu, Y., and Wang, N.-X., 2022, "Experimental and Numerical Study on Thermal Performance of a Fluoride Salt-to-Air Heat Exchanger," Ann. Nucl. Energy, **168**, p. 108876.
[17] Le Brun, N., Hewitt, G. F., and Markides, C. N., 2017, "Transient Freezing of Molten Salts in Pipe-Flow Systems: Application to the Direct Reactor Auxiliary Cooling System (DRACS)," Appl. Energy, **186**(Part 1), pp. 56–67.
[18] Tiberga, M., Shafer, D., Lathouwers, D., Rohde, M., and Kloosterman, J. L., 2019, "Preliminary Investigation on the Melting Behavior of a Freeze-Valve for the Molten Salt Fast Reactor," Ann. Nucl. Energy, **132**, pp. 544–554.
[19] Kearney, D., Herrmann, U., Nava, P., Kelly, B., Mahoney, R., Pacheco, J., Cable, R., Potrovitza, N., Blake, D., and Price, H., 2002, "Evaluation of a Molten Salt Heat Transfer Fluid in a Parabolic Trough Solar Field.," Int. Solar Energy Conf., **16893**, pp. 293–299.
[20] González-Gómez, PÁ, Petrakopoulou, F., Briongos, J. V., and Santana, D., 2017, "Steam Generator Design for Solar Towers Using Solar Salt as Heat Transfer Fluid," AIP Conf. Proc., **1850**(1), AIP Publishing.
[21] Prieto, C., Rodríguez-Sánchez, A., Ruiz-Cabañas, F. J., and Cabeza, L. F., 2019, "Feasibility Study of Freeze Recovery Options in Parabolic Trough Collector Plants Working With Molten Salt as Heat Transfer Fluid," Energies, **12**(12), p. 2340.
[22] Ozden, E., and Tari, I., 2010, "Shell Side CFD Analysis of a Small Shell-and-Tube Heat Exchanger," Energy Convers. Manage., **51**(5), pp. 1004–1014.
[23] Yang, J., and Liu, W., 2015, "Numerical Investigation on a Novel Shell-and-Tube Heat Exchanger With Plate Baffles and Experimental Validation," Energy Convers. Manage., **101**, pp. 689–696.
[24] Pal, E., Kumar, I., Joshi, J. B., and Maheshwari, N. K., 2016, "CFD Simulations of Shell-Side Flow in a Shell-and-Tube Type Heat Exchanger With and Without Baffles," Chem. Eng. Sci., **143**, pp. 314–340.
[25] Chen, Y. S., Tian, J., Zhu, H. H., Xue, J. Y., Tang, Z. F., Fu, Y., and Wang, N. X., 2019, "Thermal Sizing Design and Experimental Evaluation of Molten Salt-to-Air Heat Exchanger," Ann. Nucl. Energy, **132**, pp. 504–511.
[26] Almsater, S., Alemu, A., Saman, W., and Bruno, F., 2017, "Development and Experimental Validation of a CFD Model for PCM in a Vertical Triplex Tube Heat Exchanger," Appl. Therm. Eng., **116**, pp. 344–354.
[27] Benoit, H., Spreafico, L., Gauthier, D., and Flamant, G., 2016, "Review of Heat Transfer Fluids in Tube-Receivers Used in Concentrating Solar Thermal Systems: Properties and Heat Transfer Coefficients," Renew. Sustain. Energy Rev., **55**, pp. 298–315.
[28] Span, R., Lemmon, E. W., Jacobsen, R. T., Wagner, W., and Yokozeki, A., 2000, "A Reference Equation of State for the Thermodynamic Properties of Nitrogen for Temperatures From 63.151 to 1000 K," J. Phys. Chem. Ref. Data, **29**(6), pp. 1361–1433.
[29] "ANSYS FLUENT 12.0. Theory Guide," Last Modified 2009. https://www.afs.enea.it/project/neptunius/docs/fluent/html/ug/node1.htm. Accessed February 12, 2024.
[30] Costa, S. C., Mahkamov, K., Kenisarin, M., Ismail, M., Lynn, K., Halimic, E., and Mullen, D., 2020, "Solar Salt Latent Heat Thermal Storage for a Small Solar Organic Rankine Cycle Plant," ASME J. Energy Resour. Technol., **142**(3), p. 031203.
[31] Özden, E., 2007, "Detailed Design of Shell-and-Tube Heat Exchangers Using CFD," Master's thesis, Middle East Technical University, Ankara, Turkey. https://open.metu.edu.tr/bitstream/handle/11511/17148/index.pdf
[32] González-Roubaud, E., Pérez-Osorio, D., and Prieto, C., 2017, "Review of Commercial Thermal Energy Storage in Concentrated Solar Power Plants: Steam vs. Molten Salts," Renew. Sustain. Energy Rev., **80**, pp. 133–148.
[33] Sharma, S., and Mortazavi, M., 2023, "Pumped Thermal Energy Storage: A Review," Int. J. Heat Mass Transfer, **213**, p. 124286.
[34] TEMA, 1999, *Standards of the Tubular Exchanger Manufacturer's Association [TEMA]*, 8th ed., Section 1–5, 7–10, Tubular Exchanger Manufacturers Association, Inc., New York.
[35] Ken, A., and Maurice, S., 2021, "Heat Transfer Theory," *Surface Production Operations 5*, K. E. Arnold and M. I. Stewart, eds., Gulf Professional Publishing, pp. 361–430.
[36] Peng, B., Wang, Q. W., Zhang, C., Xie, G. N., Luo, L. Q., Chen, Q. Y., and Zeng, M., 2007, "An Experimental Study of Shell-and-Tube Heat Exchangers With Continuous Helical Baffles," ASME. J. Heat Transfer, **129**(10), pp. 1425–1431.
[37] Habib, M. A., Mobarak, A. M., Sallak, M. A., Abdel Hadi, E. A., and Affify, R. I., 1994, "Experimental Investigation of Heat Transfer and Flow Over Baffles of Different Heights," ASME J. Heat Transfer-Trans. ASME, **116**(2), pp. 363–368.
[38] Wang, X., Zheng, N., Liu, Z., and Liu, W., 2018, "Numerical Analysis and Optimization Study on Shell-Side Performances of a Shell and Tube Heat Exchanger With Staggered Baffles," Int. J. Heat Mass Transfer, **124**, pp. 247–259.
[39] Kalapala, L., and Devanuri, J. K., 2022, "Influence of Fin Parameters on Melting and Solidification Characteristics of a Conical Shell and Tube Latent Heat Storage Unit," ASME J. Energy Resour. Technol., **144**(2), p. 022002.
[40] Boulaktout, N., Mezaache, E. H., Teggar, M., Arıcı, M., Ismail, K. A., and Yıldız, Ç, 2021, "Effect of Fin Orientation on Melting Process in Horizontal Double Pipe Thermal Energy Storage Systems," ASME J. Energy Resour. Technol., **143**(7), p. 070904.